Enhanced Cooper pairing in nano-patterned metals

Masoud Mohammadi-Arzanagh,[1,*] Andrey Grankin,[1] Victor Galitski,[1] and Mohammad Hafezi[1]

[1] *Joint Quantum Institute, Department of Physics, University of Maryland, College Park, MD 20742, USA*

Nano-patterning has been shown to be a powerful tool for manipulating the vibrational modes of elastic structures, with applications such as optical-mechanical mode coupling. Inspired by these recent developments in phononic band engineering, we propose a nano-patterning scheme to enhance the superconducting transition temperature T_c in phonon-mediated nano-film superconductors, such as aluminum. Using the finite element method, we simulate the lattice vibrational modes of nano-patterned films within the Debye model. Our results show that periodic nano-patterning softens the lattice vibrational modes compared to bulk films. It also increases the density of states at high energies, resulting in a couple of percent enhancement in T_c. Moreover, we investigate connections to random matrix theory and provide an experimental design prescription to optimize nano-patterning for further enhancement of the superconducting transition temperature.

Introduction— Over the past couple of decades, there has been tremendous progress in modifying phononic band structures using nano-fabrication and nano-patterning techniques [1–9]. Periodically applied defects of certain shapes induce modifications in lattice vibrations, which in turn lead to the formation of phononic crystals. Similar to the manipulation of light in photonic crystals, this advancement opens new possibilities for precisely controlling phonon modes as desired [1]. A hallmark example of nano-patterning applications is the emergence of optomechanical crystals, where optical and mechanical mode coupling is enhanced using nano-scale periodic structures. Another example is the use of this technique to produce phononic band gaps in solids, which can suppress thermal vibrations and mitigate noise and dephasing in various physical processes [10–12]. It can also be used to control and engineer the heat capacity and thermal conductance of a material. Depending on the patterning design, thermal conductance can be either suppressed or enhanced [13–15]. The ability to manipulate lattice vibrations through two-dimensional periodic patterning, enabling control over physical properties such as optomechanical coupling, heat capacity, thermal conductivity, and thermal noise, highlights the broad applicability of nano-patterning techniques.

On another front, numerous experimental studies have demonstrated that granular superconductors, as well as thin films, often exhibit an enhanced superconducting transition temperature T_c [16–19]. This enhancement is attributed to the inherently disordered nature of granular superconductors. Specifically, the chaotic geometry of these grains has been shown to strengthen the effective electron-phonon coupling, thereby leading to a higher T_c [20]. This shows how nano-scale geometric features can enhance the transition temperature of elemental superconductors.

Motivated by such progress in nano-patterning and recent developments in the understanding of granular superconductors, it is intriguing to question whether modification of phononic band structures via nano-patterning can have an appreciable effect in phonon-induced superconductivity. Since nano-patterning length scales are usually lower bounded by 10nm, such schemes can only affect the low-energy acoustic phonons and naively one would expect that such patterning can not lead to any measurable effects. In this Letter, we investigate this question by examining the effect of nano-patterning on the lattice vibrational modes of elemental superconductors. To be concrete, we consider aluminum phononic band structure of a bulk nano-film and study its modification in the presence of nano-patterning within the Debye

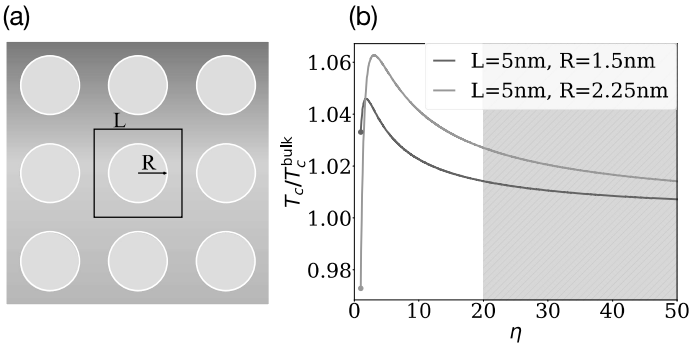

FIG. 1. **(a)** The schematic shows an aluminum nanofilm with circular holes of radius R being periodically patterned inside unit cells of side length L. **(b)** The enhancement in transition temperature as a function of the scaling factor η for the two base geometries $(L, R) = (5\,\text{nm}, 1.5\,\text{nm})$ and $(L, R) = (5\,\text{nm}, 2.25\,\text{nm})$. The perimeter-squared-to-area ratios for them are $\mathcal{L}^2/A = 4.95, 21.97$, respectively, where $\mathcal{L} = 2\pi R, A = L^2 - \pi R^2$. The base geometries are scaled such that $(L, R) \to (\eta L, \eta R)$. We observe an optimal scaling factor for each hole radius, for which the sample exhibits the highest enhancement in transition temperature. This maximum enhancement in transition temperature is higher for the geometry with greater perimeter-squared-to-area ratio. The gray dashed area represents the region where the size of the corresponding unit cell would be comparable to the superconducting coherence length $\sim$ 100nm, hence, the unit cell averaging scheme to obtain Eq. (10) would break down. The two dotted points at the beginning of each curve represent the T_c values of unscaled geometries, i.e., $\eta = 1$, with transition temperatures of $T_c/T_c^{\rm bulk} = 1.033$ for the blue curve ($R = 1.5\,\text{nm}$) and $T_c/T_c^{\rm bulk} = 0.972$ for the orange curve ($R = 2.25\,\text{nm}$).

model. We study changes in the phononic density of states and demonstrate that nano-pattering softens the low energy phonon modes. Moreover, despite considering large-length-scale nano-patterning, we demonstrate that it can influence the entire phonon spectrum and observe an increased density of states at high energies for the patterned cases compared to the bulk, as predicted by the well-known Weyl-Vasilev law [21, 22]. We benchmark our findings for the density of states per unit area against the predictions of this law and further explore its connection to chaotic grains. We then use these results to evaluate the Eliashberg function for both bulk and patterned samples and demonstrate that, for appropriate length scales, the high energy enhancement of this function in the patterned case can be used to obtain an enhancement of $\sim 6\%$ in T_c. Lastly, we propose a recipe to leverage the implications of Weyl-Vasilev law for optimizing fabrication patterns to further enhance the superconducting transition temperature.

Geometry and Phonon Model—To this end, we consider two scenarios: (1) a bulk two-dimensional aluminum nanofilm, and (2) the same sheet of aluminum, nano-patterned with periodically arranged holes of circular shapes, as illustrated in panel (a) of Fig. 1. To analyze the phonons, we use the Debye model implying a linear spectrum with cut-off. We adjust this cut-off when we pattern and call it ν_D henceforth. Moreover, we ensure the hole features are much greater than the atomic scales. [23–25]. The linear equation reads as:

$$\rho\partial_t^2 u_i = \sum_{jkl} C_{ijkl}\partial_j\partial_k u_l. \tag{1}$$

Here, ρ is the density of aluminum, $\vec{u}$ stands for the local lattice displacement, and C_{ijkl} represents aluminum's stiffness tensor. Essentially, it is a fourth-rank tensor that connects the stress and strain within a linear elastic medium. In the isotropic case, this tensor can be represented as:

$$C_{ijkl} = \lambda_{\mathrm{L}}\delta_{ij}\delta_{kl} + \mu_{\mathrm{L}}(\delta_{ik}\delta_{jl} + \delta_{il}\delta_{jk}) \tag{2}$$

where λ_{L} and μ_{L} are the first and second Lamé parameters. For the second case, where holes are patterned in a periodic order, proper boundary condition at the hole boundary must be implemented to determine the phonon modes of Eq. (1). This condition, which is called free surface boundary condition, represents that the normal forces, both shear and compression, vanish at the boundary of aluminum and vacuum:

$$\sum_{jkl} dS_j C_{ijkl}\partial_k u_l = 0 \quad \forall i \quad \in \quad 1, 2 \tag{3}$$

where $d\vec{S}$ is the normal differential length element around the hole boundary. Accompanied by Eq. (1), this boundary condition is sufficient to determine the spectrum of vibration modes.

As well known for eigenvalues of Laplace operator, the boundary condition affects the asymptotic behavior of the density of states. In particular, Weyl's law establishes positive/negative correction for Neumann/Dirichlet boundary conditions, respectively [21]. Weyl's law has been explored for Eq. (1) with the free surface boundary condition, and the phonon spectrum exhibits a positive correction to the phonon density of states per unit area in a chaotic grain relative to the bulk case [21, 22, 26]:

$$\mathcal{N}(\nu) - \mathcal{N}_{\mathrm{bulk}}(\nu) = \frac{\beta_p \mathcal{L}}{2Ac_s}\nu, \tag{4}$$

where $\mathcal{N}(\nu)$ is the number of states per unit area with energy below energy $h\nu$ for the grain, and $\mathcal{N}_{\mathrm{bulk}}(\nu)$ is the corresponding quantity for the bulk geometry. Here, β_p is an analytical constant with a value of $\beta_p = 2.085$ for aluminum [26]. $\mathcal{L}$ represents the perimeter of the grain, and A denotes its area. c_s is the transverse sound velocity of aluminum, and ν is the cyclic frequency at which $\mathcal{N}$ is evaluated. In this work, we numerically demonstrate that the same expression holds for our periodically patterned hole geometry. Specifically, in our geometry Eq. (4) holds with $\mathcal{L}$ being the perimeter of the circle patterned inside the unit cell, and A denotes the area of the unit cell excluding the area of the circle. Applying the Migdal-Eliashberg theory, we further show that this positive correction to the density of states can enhance the Eliashberg function and effective electron-phonon coupling. This, in turn, leads to an enhancement of the superconducting transition temperature.

Electron-Phonon Coupling—Having discussed the effect of nano-patterning on the phonon spectrum, we move on to addressing how this modification can be incorporated into the electronic aspect of the system. To achieve this, we need to introduce a model that captures the coupling of electrons to the lattice vibration modes. The simplest and most practical model for this purpose is the Hamiltonian introduced by Fröhlich [27–29]:

$$H = \sum_{l\vec{q}} E_{l,\vec{q}} a^\dagger_{l,\vec{q}} a_{l,\vec{q}} + \sum_{k,\sigma=\uparrow,\downarrow} \xi_{\vec{k}} \psi^\dagger_{\sigma\vec{k}} \psi_{\sigma\vec{k}} + g\sum_{\sigma=\uparrow,\downarrow} \int \chi(\vec{r})\psi^\dagger_\sigma(\vec{r})\psi_\sigma(\vec{r})d\vec{r}, \tag{5}$$

where the first two terms represent the free Hamiltonians of the phonons and electrons, respectively, while the last term describes the coupling between them. g represents the electron-phonon coupling strength, and $\chi(\vec{r})$ is defined as [28]:

$$\chi(\vec{r}) = \sum_{l\vec{q}} \frac{\nabla\cdot\vec{V}_{l,\vec{q}}}{\sqrt{2E_{l,\vec{q}}}}(a_{l,\vec{q}} + a^\dagger_{l,-\vec{q}}), \tag{6}$$

where $E_{l,\vec{q}}$ and $a^\dagger_{l,\vec{q}}(a_{l,\vec{q}})$ are the phonon energy and creation (annihilation) operator of the l^{th} band with Bloch wave vector $\vec{q}$, i.e. $q_x, q_y \in [-\pi/L, \pi/L]$. $\xi_{\vec{k}}$ is the electron's dispersion and $\psi^\dagger_\sigma(\vec{r})$ is the creation operator of an electron at position $\vec{r}$. Mediated by phonons, the electrons experience an attractive potential, which pairs them up

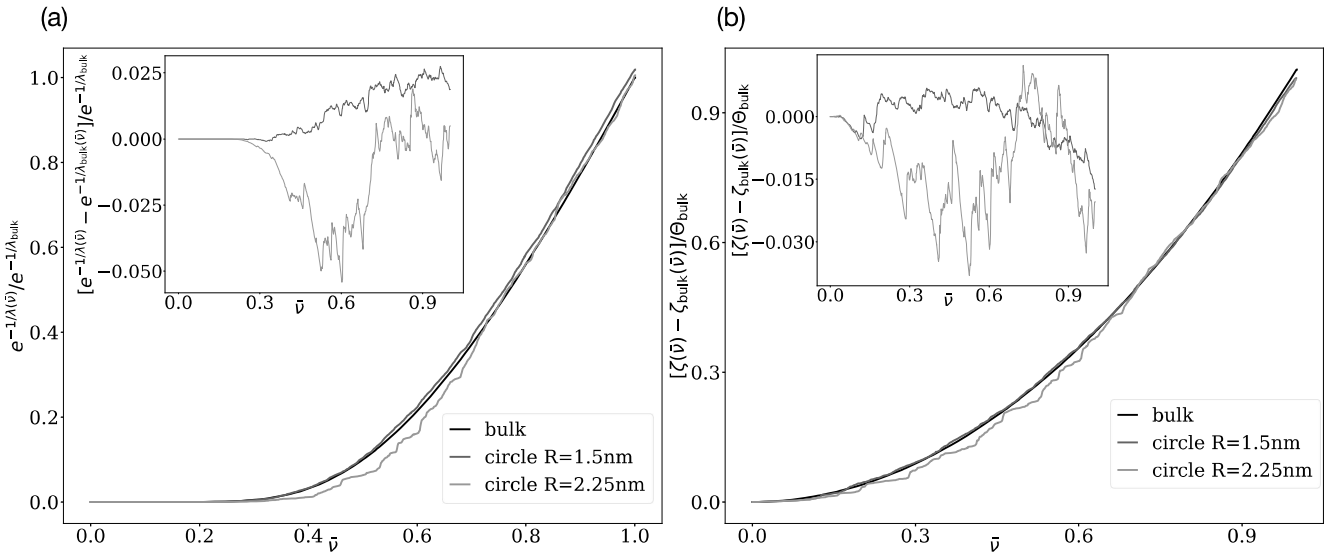

FIG. 2. **(a)** The $e^{-1/\lambda(\bar{\nu})}/e^{-1/\lambda_{\rm bulk}}$ function for the unpatterned sample and the patterned samples with two different radii, $R = 1.5\,\text{nm}$ and $R = 2.25\,\text{nm}$, are plotted in black, blue, and orange, respectively, as a function of the dimensionless frequency ratio $\bar{\nu} = \nu/\nu_D$. The inset represents the difference of the blue and orange curve from the black in the entire domain of the plot. As it is more clear from the difference plot, the blue curve ends up having a larger Eliashberg parameter λ than that of the bulk case $\lambda_{\rm bulk}$, while the orange does not show a sensible increase in this parameter compared to the bulk. **(b)** The corresponding $\zeta(\bar{\nu})/\Theta_{\rm bulk}$ function for each of the geometries discussed in panel (a) are plotted as a function of dimensionless frequency ratio $\bar{\nu} = \nu/\nu_D$. Once again, the inset represents the difference of the blue and orange curve from the black. Both of the curves have a smaller average frequency $\Theta = \zeta(\nu_D)$ than that of the bulk.

into the superconducting state below the superconducting transition temperature [30]. To find the critical temperature, we apply Migdal-Eliashberg theory, and estimate its solution for the transition temperature using McMillan's formula, where we perform the Fermi surface averaging of the phononic propagator [31]:

$$k_B T_c = \frac{h\Theta}{1.2} \exp\left[-\frac{1.04(1+\lambda)}{\lambda - \mu^*(1+0.62\lambda)}\right]. \tag{7}$$

Here, k_B and h are the Boltzmann and Planck constants, respectively. μ^* is a parameter representing the Coulomb repulsion, for which $\mu^* = 0.1$ is a good approximation [32, 33]. It is worth noting that we do not take the effect of nano-patterning on μ^* into account. λ and Θ are defined through electron phonon spectral function as the following:

$$\lambda(\nu) = 2\int_0^{\nu} \frac{\alpha^2F(\nu')}{\nu'} d\nu', \tag{8}$$

$$\zeta(\nu) = \frac{2}{\lambda(\nu_D)} \int_0^{\nu} \alpha^2F(\nu') d\nu', \tag{9}$$

where $\lambda = \lambda(\nu_D), \Theta = \zeta(\nu_D)$, and ν_D is the Debye cut-off frequency of the system in consideration. The electron phonon spectral function (Eliashberg function), $\alpha^2F(\nu)$, is the weight through which Θ and λ are defined. It plays a key role in the determination of the transition temperature of superconductors, and provides a detailed description of the interaction between electrons and phonons, which is essential for accurately modeling superconducting properties [34]. For the particular periodic geometry considered in this work this function reads as:

$$\alpha^2F(\nu) = \tilde{g}\sum_{ml}\int d^2q \frac{1}{2E_{l,\vec{q}}} \frac{|\alpha_{l,\vec{q}}(\vec{K}_m)|^2 \delta(h\nu - E_{l,\vec{q}})}{|\vec{q}+\vec{K}_m|\sqrt{1-\frac{|\vec{q}+\vec{K}_m|^2}{4k_F^2}}}, \tag{10}$$

where we have defined:

$$\tilde{g} = \frac{g^2 N(0)}{4\pi^2 k_F}. \tag{11}$$

Here, $E_{l,\vec{q}}$ is the phonon energy of the $l^{\rm th}$ band at Bloch wave vector $\vec{q}$, and $\vec{K}_m = \frac{2\pi}{L}(m_x\hat{x} + m_y\hat{y})$ with m_x, m_y being arbitrary integers. k_F denotes the electronic Fermi wave number and $N(0)$ is the electronic density of states at the Fermi surface. $\alpha_{l,\vec{q}}(\vec{K}_m)$ are the Fourier coefficients of the periodic Bloch amplitude of the $\nabla \cdot \vec{V}_{l,\vec{q}}$ function, where $\vec{V}_{l,\vec{q}}(\vec{r})$ is the full phonon wave function of the $l^{\rm th}$ band at Bloch wave vector $\vec{q}$. A detailed derivation of spectral function for our patterned geometry is provided in appendix A. We determine $\tilde{g}$ by applying Eq. (10) to the bulk geometry, extracting the parameters required for McMillan's formula, and fitting T_c to match the known transition temperature of bulk aluminum. Finding $\tilde{g}$ enables us to calculate the corresponding parameters for the patterned geometry, evaluate its transition temperature, and compare it with the bulk value.

Results and Conclusion—We begin the discussion of the results by benchmarking the modification of the density of states per unit area against the implications of

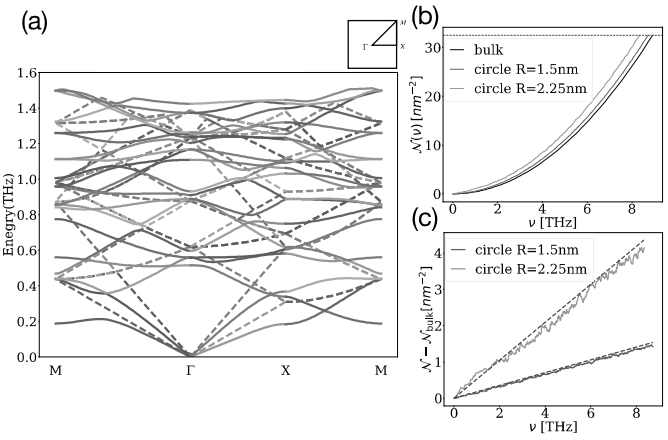

FIG. 3. **(a)** The phononic band structure for both the bulk and nano-patterned samples, displaying the first 20 bands. Dashed lines represent the bulk sample, while solid lines correspond to the sample patterned with circular holes of radius $R = 1.5\,\text{nm}$ and a unit cell size of $L = 5\,\text{nm}$. Nano-patterning is observed to soften the phonon mode, thereby increasing the phonon density of states. The inset on the upper right corner illustrates the Brillouin zone with respect to which the band structure is plotted. **(b)** The phonon's cumulative density of states per unit area (i.e., the number of eigenstates below a certain energy) for the bulk sample and two patterned samples with radii $R = 1.5\,\text{nm}$ and $R = 2.25\,\text{nm}$. The dashed red horizontal line represents the value that corresponds to the total number of states per unit area for the bulk case; the Debye energy of the two other geometries are modified to stay consistent with this value, i.e., $\mathcal{N}_{\text{bulk}}(\nu_D^{\text{bulk}}) = \mathcal{N}(\nu_D)$. **(c)** The difference in cumulative density of states per unit area between the unpatterned sample and the two patterned samples with the same radii as in panel b, as a function of frequency. The dashed lines represent the analytic prediction for high energies based on Weyl-Vasilev law [26]. The geometry with a higher perimeter-squared-to-area ratio exhibits a greater enhancement of the density of states per unit area.

Weyl-Vasilev law for high energies [21, 26]. In particular, as shown in panel (c) of Fig. 3, we have plotted $\mathcal{N}(\nu) - \mathcal{N}_{\text{bulk}}(\nu)$ as a function of frequency. The linearity of this plot and its slope show good agreement with the analytic prediction of Eq. (4) at high energies, and the geometry with a greater perimeter squared-to-area ratio exhibits a higher enhancement of the density of states per unit area. This increase for high energies translates to an enhancement in the Eliashberg function at the same energy region as well, since both are affected by the same geometric factors. To be more concrete, as evident from the behavior of $\lambda(\nu)$ and $\zeta(\nu)$ with respect to frequency in panel (a) and (b) of Fig. 2, there is a competition between low-energy suppression and high-energy enhancement in these functions. For the two specific patterned geometries considered in Fig. 2, $(L, R) = (5\,\text{nm}, 1.5\,\text{nm})$ (blue) and $(L, R) = (5\,\text{nm}, 2.25\,\text{nm})$ (orange), whose enhancements in T_c correspond to the blue and orange dots in panel (b) of Fig. 1, the following observations can be made: For the blue curve $(L, R) = (5\,\text{nm}, 1.5\,\text{nm})$, despite the low-energy suppression, the high-energy enhancement dominates, resulting in an increase in the transition temperature. However, for the orange curve $(L, R) = (5\,\text{nm}, 2.25\,\text{nm})$, low-energy suppression prevails, leading to a decrease in transition temperature. Nevertheless, in what follows we show that scaling the size of the unit cell and circle proportionately can suppress the low-energy decrease in these functions and leverage the high-energy increase in them to enhance the transition temperature. This results in an overall enhancement of T_c for both geometries, with the geometry having a greater perimeter-squared-to-area ratio showing an advantage due to a faster increase of the Eliashberg function at high energies.

We continue the discussion of the results with a brief explanation of our scaling scheme. The linearity of the phonon equations implies that $\mathcal{N}(\eta L, \eta R, \nu) \sim \mathcal{N}(L, R, \eta\nu)$. Assuming $1/k_F$ is much smaller than the other length scales in the problem, it also follows that $\alpha^2F(\eta L, \eta R, \nu) \sim \alpha^2F(L, R, \eta\nu)$. This approach enables us to determine the density of states per unit area and the Eliashberg function for scaled geometries without the need to repeat the full phononic band structure simulation (see appendix B for further details). As an example, considering the two scaled geometries with $(L, R) = (15\text{nm}, 4.5\text{nm})$ and $(L, R) = (15\text{nm}, 6.75\text{nm})$, we obtain the modified parameters $\lambda/\lambda_{\text{bulk}} = 1.011$, $\Theta/\Theta_{\text{bulk}} = 0.987$, $\nu_D/\nu_D^{\text{bulk}} = 0.992$ for the former case and $\lambda/\lambda_{\text{bulk}} = 1.019$, $\Theta/\Theta_{\text{bulk}} = 0.972$, $\nu_D/\nu_D^{\text{bulk}} = 0.979$ for the latter. These ratios translate to an enhancement of $\delta T_c/T_c = 4.2\%$ and 6.3% in the transition temperature for the two scaled geometries, respectively. A plot of transition temperature enhancement as a function of scaling factor is included in panel b of Fig. 1; i.e. the geometry is scaled with a factor η such that $(L, R) \to (\eta \times L, \eta \times R)$. This plot shows that there exists an optimal scaling factor η for any base geometry for which T_c is maximized, and the geometry with a higher perimeter squared-to-area ratio has a greater maximum enhancement. Having said that, it is clear that circles are not the best choice of patterning in terms of getting a greater transition temperature, and shapes like fractals that have higher perimeter-squared-to-area ratio would give even higher enhancement in T_c. However, it is crucial to consider that the fineness of the features in the geometry must not fall below the atomic scale of the underlying material. Due to computational complexities we do not include more complex shapes in the current work. Nevertheless, the goal of this Letter is to illustrate the trend in T_c enhancement and to demonstrate the significant role that nano-patterning plays in improving the superconducting transition temperature of 2D materials, such as aluminum nano-films.

In this work, we focused on simple circular hole patterning. A clear direction for future work is to optimize the patterning shape and size to further enhance T_c, using machine learning techniques [35]. In addition, a more realistic model for phonons could be developed by accounting for the lattice structure of the underlying material and solving for the phonon modes. This approach would automatically handle the Debye cut-off frequency. Other exciting directions for future research include replacing aluminum with

other phonon-mediated superconductors, such as niobium, and exploring the potential of inducing superconductivity in non-superconducting materials.

Acknowledgment— This work was supported by DARPA HR001124-9-0310.

* masoudma@umd.edu

[1] M. Eichenfield, J. Chan, R. M. Camacho, K. J. Vahala, and O. Painter, Optomechanical crystals, nature **462**, 78 (2009).

[2] A. H. Safavi-Naeini and O. Painter, Design of optomechanical cavities and waveguides on a simultaneous bandgap phononic-photonic crystal slab, Optics express **18**, 14926 (2010).

[3] T. J. Kippenberg and K. J. Vahala, Cavity optomechanics: back-action at the mesoscale, science **321**, 1172 (2008).

[4] M. Eichenfield, J. Chan, A. H. Safavi-Naeini, K. J. Vahala, and O. Painter, Modeling dispersive coupling and losses of localized optical and mechanical modes in optomechanical crystals, Optics express **17**, 20078 (2009).

[5] I. Favero and K. Karrai, Optomechanics of deformable optical cavities, Nature Photonics **3**, 201 (2009).

[6] R. H. Olsson and I. El-Kady, Microfabricated phononic crystal devices and applications, Measurement science and technology **20**, 012002 (2008).

[7] J. O. Vasseur, A.-C. Hladky-Hennion, B. Djafari-Rouhani, F. Duval, B. Dubus, Y. Pennec, and P. Deymier, Waveguiding in two-dimensional piezoelectric phononic crystal plates, Journal of applied physics **101** (2007).

[8] K. Gu, C.-L. Chang, and J.-C. Shieh, Design and fabrication of 2d phononic crystals in surface acoustic wave micro devices, in *ASME International Mechanical Engineering Congress and Exposition*, Vol. 4224 (2005) pp. 593–596.

[9] S. Mohammadi, A. A. Eftekhar, A. Khelif, W. D. Hunt, and A. Adibi, Evidence of large high frequency complete phononic band gaps in silicon phononic crystal plates, Applied Physics Letters **92** (2008).

[10] O. Florez, G. Arregui, M. Albrechtsen, R. C. Ng, J. Gomis-Bresco, S. Stobbe, C. M. Sotomayor-Torres, and P. D. García, Engineering nanoscale hypersonic phonon transport, Nature Nanotechnology **17**, 947 (2022).

[11] M. Sigalas and E. N. Economou, Band structure of elastic waves in two dimensional systems, Solid state communications **86**, 141 (1993).

[12] M. S. Kushwaha, P. Halevi, L. Dobrzynski, and B. Djafari-Rouhani, Acoustic band structure of periodic elastic composites, Physical review letters **71**, 2022 (1993).

[13] T. Gorishnyy, C. K. Ullal, M. Maldovan, G. Fytas, and E. Thomas, Hypersonic phononic crystals, Physical review letters **94**, 115501 (2005).

[14] R. Anufriev and M. Nomura, Phonon engineering for quantum hybrid systems, in *Quantum Hybrid Electronics and Materials* (Springer, 2022) pp. 15–24.

[15] M. Nomura, Phononic band engineering for thermal conduction control and similarity with photonic band engineering, Microsystem Technologies **22**, 473 (2016).

[16] B. Abeles, R. W. Cohen, and G. Cullen, Enhancement of superconductivity in metal films, Physical Review Letters **17**, 632 (1966).

[17] R. W. Cohen and B. Abeles, Superconductivity in granular aluminum films, Physical Review **168**, 444 (1968).

[18] M. Strongin, O. Kammerer, J. Crow, R. Parks, D. Douglass Jr, and M. Jensen, Enhanced superconductivity in layered metallic films, Physical Review Letters **21**, 1320 (1968).

[19] S. Prischepa and V. Kushnir, Phonon softening in nanostructured phonon–mediated superconductors, Journal of Physics: Condensed Matter **35**, 313003 (2023).

[20] A. Grankin, M. Hafezi, and V. Galitski, Enhanced cooper pairing via random matrix phonons in superconducting grains, arXiv preprint arXiv:2408.03927 (2024).

[21] H. Weyl, Über die asymptotische verteilung der eigenwerte, Nachrichten von der Gesellschaft der Wissenschaften zu Göttingen, Mathematisch-Physikalische Klasse **1911**, 110 (1911).

[22] D. G. Vasil'ev, Asymptotic behavior of the spectrum of a boundary value problem, Trudy Moskovskogo Matematicheskogo Obshchestva **49**, 167 (1986).

[23] L. D. Landau, L. Pitaevskii, A. M. Kosevich, and E. M. Lifshitz, *Theory of elasticity: volume 7*, Vol. 7 (Elsevier, 2012).

[24] F. W. Hehl and Y. Itin, The cauchy relations in linear elasticity theory, Journal of elasticity and the physical science of solids **66**, 185 (2002).

[25] J. Marsden and T. Hughes, J., r. mathematical foundations of elasticity dover publications (1994).

[26] P. Bertelsen, C. Ellegaard, and E. Hugues, Distribution of eigenfrequencies for vibrating plates, The European Physical Journal B-Condensed Matter and Complex Systems **15**, 87 (2000).

[27] H. Fröhlich, Electrons in lattice fields, Advances in Physics **3**, 325 (1954).

[28] A. A. Abrikosov, L. P. Gorkov, and I. E. Dzyaloshinski, *Methods of Quantum Field Theory in Statistical Physics* (Courier Corporation, 2012).

[29] A. Altland and B. D. Simons, *Condensed matter field theory* (Cambridge university press, 2010).

[30] L. N. Cooper, Bound electron pairs in a degenerate fermi gas, Physical Review **104**, 1189 (1956).

[31] We use cyclic frequency throughout the work.

[32] P. B. Allen and R. Dynes, Transition temperature of strong-coupled superconductors reanalyzed, Physical Review B **12**, 905 (1975).

[33] W. McMillan, Transition temperature of strong-coupled superconductors, Physical Review **167**, 331 (1968).

[34] S. K. Bose and J. Kortus, Electron-phonon coupling in metallic solids from density functional theory, Vibronic and Electron-Phonon Interactions and Their Role in Modern Chemistry and Physics , 1 (2009).

[35] V. Lopez-Pastor and F. Marquardt, Self-learning machines based on hamiltonian echo backpropagation, Physical Review X **13**, 031020 (2023).

[36] We use cyclic frequency throughout the work.

[37] We use cyclic frequency throughout the work.

[38] We use cyclic frequency throughout the work.

Appendix A: The derivation of Eliashberg function

In the absence of translation invariance, the phonon propagator and the two body electron-electron interaction, which is mediated by phonons, are not necessarily functions of coordinated difference. Therefore, we can write the following general form for the phonon mediated electron-electron interaction:

$$D(r,r';\epsilon_n) = g^2 \sum_{l\vec{q}} \frac{1}{2E_{l,\vec{q}}} \phi_{l,\vec{q}}(\vec{r})\phi^*_{l,\vec{q}}(\vec{r}') \frac{2E_{l,\vec{q}}}{E^2_{l,\vec{q}} + \epsilon_n^2} \quad \text{(A1)}$$

Here, g is a dimensionfull constant determining the electron-phonon coupling strength, $E_{l,\vec{q}}$ is the energy of the l^{th} band with Bloch wave vector $\vec{q}$, and $\phi_{l,\vec{q}}(\vec{r})$ is the divergence of the corresponding phonon wave function:

$$\phi_{l,\vec{q}}(\vec{r}) = \nabla \cdot \vec{V}_{l,\vec{q}}(\vec{r}), \tag{A2}$$

where $\vec{V}_{l,\vec{q}}$s are the full phonon wave functions for l^{th} band and Bloch wave vector $\vec{q}$. Using Bloch's theorem we can write the function $\phi_{l,\vec{q}}(\vec{r})$ in the following form:

$$\phi_{l,\vec{q}}(\vec{r}) = \varphi_{l,\vec{q}}(\vec{r}) e^{i\vec{q}\vec{r}}. \tag{A3}$$

Once again, $\vec{q}$ is the Bloch wave vector in the first Brillouin zone, and $\varphi_{l,\vec{q}}(r)$ is the periodic amplitude that can be expanded in the Fourier basis:

$$\varphi_{l,\vec{q}}(\vec{r}) = \sum_m \alpha_{l,\vec{q}}(\vec{K}_m) e^{i\vec{K}_m.\vec{r}}. \tag{A4}$$

Here, $\vec{K}_m = \frac{2\pi m_x}{L}\hat{x} + \frac{2\pi m_y}{L}\hat{y}$ with m_x, m_y being arbitrary integers and L being the side length of the unit cell. Substituting this in the phonon propagator and expressing it in terms of the relative $\vec{r} - \vec{r}' = \vec{\ell}$ and center of mass coordinates $\vec{R} = \frac{\vec{r}+\vec{r}'}{2}$ yields:

$$\begin{aligned} D(\vec{R}, \vec{\ell}; \epsilon_n) &= g^2 \sum_{l\vec{q}} \frac{1}{2E_{l,\vec{q}}} \phi_{l,\vec{q}}(\vec{r}) \phi^*_{l,\vec{q}}(\vec{r}') \frac{2E_{l,\vec{q}}}{E^2_{l,\vec{q}} + \epsilon_n^2} \\ &= g^2 \sum_{lkmm'} \frac{1}{E^2_{l,\vec{q}} + \epsilon_n^2} \alpha_{l,\vec{q}}(\vec{K}_m) \alpha^*_{l,\vec{q}}(\vec{K}'_m) \\ &\quad e^{i[\vec{q} + \frac{1}{2}(\vec{K}_m + \vec{K}_{m'})]\cdot\vec{\ell}} e^{i(\vec{K}_{m'} - \vec{K}_m)\cdot\vec{R}}. \end{aligned} \tag{A5}$$

This expression does not have translation invariance, but, averaging over the unit cell removes the dependence on center of mass coordinate $\vec{R}$ and the result is only a function of difference. This is a justified step due to the fact that superconducting coherence length is much larger than the unit cell size that we are considering in this work. Performing the integration over $\vec{R}$ then yields:

$$\begin{aligned} \bar{D}(\vec{\ell}, \epsilon_n) &= g^2 \sum_{l\vec{q}\vec{K}_m} \frac{1}{E^2_{l,\vec{q}} + \epsilon_n^2} \left|\alpha_{l,\vec{q}}(\vec{K}_m)\right|^2 e^{i(\vec{q}+\vec{K}_m).\vec{\ell}} \\ &= \sum_{\vec{k}} \bar{D}(\vec{k}, \epsilon_n) e^{i\vec{k}.\vec{\ell}}, \end{aligned} \tag{A6}$$

where $\vec{k} = \vec{q} + \vec{K}_m$ is the momentum that electrons gain via scattering off of phonons. We use this result and combine it with the already existing expression for the Eliashberg function in the literature [34], to get the Eliashberg function for our geometry:

$$\alpha^2 F(\nu) = \tilde{g} \sum_{ml} \int d^2q \frac{1}{2E_{l,\vec{q}}} \frac{|\alpha_{l,\vec{q}}(\vec{K}_m)|^2 \delta(h\nu - E_{l,\vec{q}})}{|\vec{q} + \vec{K}_m| \sqrt{1 - \frac{|\vec{q}+\vec{K}_m|^2}{4k_F^2}}}, \tag{A7}$$

where:

$$\tilde{g} = \frac{g^2 N(0)}{4\pi^2 k_F}. \tag{A8}$$

Here, k_F is the Fermi wave vector, and $N(0)$ is the electronic density of states at the Fermi surface. We evaluate the above expression by solving for the phonon spectrum using commercially available software to obtain $V_{l,\vec{q}}(r)$, and then taking the Fourier transform of its divergence to find $\alpha_{l,\vec{q}}(\vec{K}_m)$.

Appendix B: Numerical fitting for high energy part of $\alpha^2F(\nu), \lambda(\nu)$

Similar to the high-energy part of the cumulative density of states per unit area, where the Weyl-Vasilev law predicts a linear positive correction,

$$\mathcal{N}(\nu) - \mathcal{N}_{\text{bulk}}(\nu) = \frac{\beta_p \mathcal{L}}{2Ac_s}\nu,$$

we expect the high-energy part of the cumulative Eliashberg function, $\int_0^\nu \alpha^2F(\nu')d\nu'$, to exhibit a similar behavior for the two geometries under consideration [20]:

$$\int_0^\nu \left[\alpha^2F(\nu') - \alpha^2F_{\text{bulk}}(\nu')\right] d\nu' = s\nu.$$

Where s is the slope of linear correction. Consequently, the

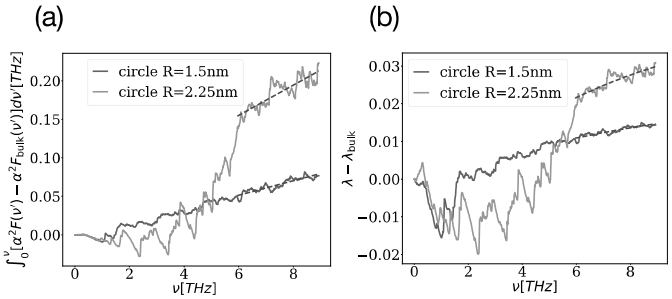

FIG. 4. **(a)** The difference in the Eliashberg function between the bulk and patterned samples with radii of $R = 1.5\,\text{nm}$ and $R = 2.25\,\text{nm}$, as a function of frequency. The high-energy region of both curves exhibits linear behavior, with the slope determined via numerical linear fitting. This linear fit is utilized to estimate the Eliashberg function for similarly scaled geometries, i.e., geometries where all lengths are scaled while keeping their ratios fixed. **(b)** The difference in λ between the bulk and patterned samples, with radii of $R = 1.5\,\text{nm}$ and $R = 2.25\,\text{nm}$, plotted as a function of frequency. Given the linear behavior of the difference in the Eliashberg function at high energies in panel a, the high-energy part of both curves in this plot is expected to exhibit logarithmic behavior. The dashed green curves represent the logarithmic numerical fit. Like in panel a, these fits are used to estimate λ for scaled geometries where all lengths are increased proportionally while keeping their ratios fixed.

high-energy part of $\lambda(\nu) - \lambda_{\text{bulk}}(\nu)$ is expected to exhibit a logarithmic behavior. In panels (a) and (b) of Fig. 4, we have plotted these deviations from the bulk values alongside their numerical fits as functions of frequency. The slope of the linear fit and the parameters of the logarithmic fit were determined using numerical packages. In fact, the

cumulative Eliashberg function $\int_0^\nu \alpha^2F(\nu')d\nu'$, and $\lambda(\nu)$ exhibit similar positive high energy correction with respect to the bulk for the patterned samples. As shown in Fig. 4, the geometry with a higher perimeter squared-to-area ratio shows a greater increase in both of these functions at high energies. The numerical fits (green dashed curves) allow us to extrapolate these functions and find the corresponding values at any higher energy of interest. These values are used to find the Eliashberg parameters of scaled geometries. By scaling to larger geometries, the enhancement of these functions at high energies can be leveraged to counteract the low energy suppression, that is discussed in the main text and in Fig. 2.